Synchrotron High-Energy X-ray & Neutron Diffraction, and Laser-Scanning Confocal Microscopy: *In-Situ* Characterization Techniques for Bulk Nanocrystalline Metals

Megumi Kawasaki^{1,*}, Jae-Kyung Han¹, Xiaojing Liu^{2,3}, Suk-Chun Moon⁴ and Klaus-Dieter Liss^{4,*}

This report is aimed at giving an overview of the significance of the novel and innovative microstructural and microscopic characterization techniques for bulk nanostructured metals processed by severe plastic deformation, specifically high-pressure torsion (HPT). In practice, the microstructural relaxation behavior upon heating of nanostructured 316L stainless steel and CoCrFeNi high-entropy alloy was characterized by *in-situ* heating neutron diffraction measurements; the heterogeneous phase distribution of an HPT-bonded hetero-nanostructured Al–Mg alloy was examined using synchrotron high-energy X-ray diffraction; and the microstructural evolution upon heating of a nanostructured CoCrFeNiMn high-entropy alloy was examined by laser-scanning confocal microscopy. These novel techniques are complementary to each other and any other *in-* or *ex-situ* testing methods, especially when nanocrystalline metals are transforming microstructurally and compositionally with temperature and time in a hierarchical manner. The outcomes of the studies emphasize the importance of the methodologies and the development of characterization techniques for further in-depth exploration in the research field of severe plastic deformation.

[doi:10.2320/matertrans.MT-MF2022022]

(Received January 31, 2023; Accepted April 27, 2023; Published May 26, 2023)

Keywords: high-pressure torsion, laser-scanning confocal microscopy, nanocrystalline metals, neutron diffraction, synchrotron high-energy X-rays

1. Introduction

Bulk nanostructured metals and their processing techniques of severe plastic deformation (SPD) have raised awareness from the materials research community because of their superior mechanical and functional properties and material processing capability, respectively. A continuous effort has been made in the research field dealing with the processing of nanostructured materials and a significant number of studies have been conducted to understand the underlying mechanisms that control the mechanical behaviors and further functionality of such materials. 1) However, microstructural changes from and to nanostructure with time and temperature, i.e., under heating, are evaluated based on ex-situ type measurements, and the continuous and dynamic changes of microstructure are often difficult to be captured by the generally available lab facility. Moreover, while complex nanostructures involving numerous defects have been investigated by various microscopy techniques with high magnifications, 2-5) it leaves a question of how the heterogeneous nanostructure in bulk metals evolves with time, temperature, etc. It suggests the necessity of the application of novel characterization techniques that enable us to understand the microstructural evolution on an additional scale, such as time, temperature, and length (or

Evolution in nanostructure can be evaluated in reciprocal space using diffraction such as X-ray, synchrotron, and neutron diffraction. Lab-scale X-ray diffraction (XRD) and

their line profile analysis have been used for investigating the microstructural evolution and phase transformation of the SPD-processed nanocrystalline metals. 6-9) The limited penetration depth of the reflection-type XRD¹⁰⁾ provided an opportunity to reveal microstructural heterogeneity in the nanocrystalline metals processed by SPD, especially after high-pressure torsion (HPT). In practice, the different information of microstructure and its evolution within the same sample was shown on different disk surface regions (local or global) of Mg ZK60A¹¹⁾ and separate disk surface planes taken at different disk heights (near surface or mid-section after mechanical removal of material) of a TiAl intermetallic compound. 12) Accordingly, the novel diffraction techniques using synchrotron and neutron radiation can be an alternative and complementary approach, besides any microscopic characterization, for further understanding of heterogeneity in nanostructure over multiplelength scales.

Synchrotron X-ray and neutron diffraction techniques are complementary to each other, where one can measure what the other cannot, while both provide essential structural and dynamic microstructural changes. [13] Especially high-energy X-rays can penetrate millimeters of metals and probe locally with a fine beam, [14] while neutrons integrate over a large volume. Moreover, neutrons show different diffraction contrasts, which may be sensitive to order and disorder, particularly in titanium alloys. [13,15] Representative examples of utilizing the synchrotron X-ray and neutron diffraction techniques on SPD-processed nanostructured materials [12,16–46] are listed in Table 1. Specifically, the benefits of employing these diffraction techniques on bulk nanocrystalline materials are:

¹School of Mechanical, Industrial and Manufacturing Engineering, Oregon State University, Corvallis, OR 97331, U.S.A.

²Department of Materials Science and Engineering, Technion – Israel Institute of Technology, Haifa 32000, Israel

³Materials Science and Engineering Department, and Guangdong Provincial Key Laboratory of Materials and Technologies for Energy Conversion, Guangdong Technion – Israel Institute of Technology, Shantou, Guangdong 515063, China

⁴School of Mechanical, Materials, Mechatronic and Biomedical Engineering, University of Wollongong, NSW 2522, Australia

^{*}Corresponding authors, E-mail: megumi.kawasaki@oregonstate.edu, kdl@uow.edu.au, liss@kdliss.de

Table 1 Representative examples of utilizing the synchrotron X-ray and neutron diffraction techniques on SPD-processed nanostructured materials.

Technique	Test sample	SPD techniques [§] / processing condition	Measurement /outcome	Additional measurement conditions	Reference
Synchrotron	Ti-47Al	Back-pressure ECAP powder consolidation (903K, 200 MPa)	Phase transformation, thermal lattice expansion	In-situ heating & cooling (300-1075 K at 3 & 5 K/min)	Liss <i>et al</i> . 2009 ¹⁶⁾
Synchrotron	Cu-2.5Ni- 0.6Si	- ECAP (8 passes, route B _C at 423 K) - HPT (10 turns, 6 GPa, RT, 1 rpm)	Precipitation kinetics	In-situ aging (823 and 973 K up to 1080 min)	Azzeddine et al. 2014 ¹⁷⁾
Synchrotron	Ti-16.1Nb	HPT (0, 1, 5 and 10 turns at 4 and 8 GPa, RT) with and without annealing (623 and 793 K)	Phase change	-	Panigrahi <i>et al.</i> 2015 ¹⁸⁾
Synchrotron	Al6061-T6	ECAP (1 pass, RT)	Texture, residual stress	-	Reyes-Ruiz et al 2016 ¹⁹⁾
Synchrotron	Pure Ni	ARB (equivalent strain = 4.8)	Lattice plane strain, Dislocation density	In-situ tensile (8.3 × 10 ⁻³ s ⁻¹ , RT)	Adachi <i>et al.</i> 2016 ²⁰⁾
Synchrotron	Ti	HPT (up to 6 GPa, shear strain of 0.5, 2.7, 6.4 and ~21)	Phase transformation, microstructural parameters	In-situ HPT	Schafler <i>et al</i> . 2017 ²¹⁾
Synchrotron	Cu-Ag, Cu-Co	HPT powder consolidation (5-100 turns, 7.8 GPa, 0.2 and 0.6 rpm, RT and 373-573 K)	Phase change	-	Kormout <i>et al</i> . 2018 ²²⁾
Synchrotron	TiZrNbHfTa	HPT (5 turns, 7.8 GPa, 0.2) rpm, RT) + annealing (1 h at 573-1373 K, or 5 min – 100 h at 773 K)	Phase change	-	Schuh <i>et al.</i> 2018 ²³⁾
Synchrotron	Cu-Ag, Cu-Sn	HPT (5 turns, 6 GPa, 0.9 s ⁻¹) + annealing (773, 873 and 1073 K)	Phase change, lattice parameter	-	Straumal et al. 2020 ²⁴⁾
Synchrotron	Cu-Co, Cu-Fe	HPT powder consolidation (100 turns for \$\phi 8\$ mm, 250 turns for \$\phi 30\$ mm, RT)	Texture, phase transformation	In-situ heating (up to 763 K)	Wurster <i>et al.</i> 2020 ²⁵⁾
Synchrotron	CoCuFeMnNi	HPT (0.1, 0.5, 1 and 5 turns, 5 GPa, RT)	Texture	Position-sensitive (1 mm step size	Sonkusare et al.
Synchrotron	Ti-15Mo	HPT (1 turn, 7 GPa, RT)	Phase transformation	along HPT disk radius) In-situ heating (5 K/min to 923 K)	2020 ²⁶⁾ Bartha <i>et al</i> .
Synchrotron	Si (100) wafer	HPT (10 turns, 24 GPa, RT, 1 rpm)	Phase transformation	Position-sensitive (HPT disk center & edge), in-situ heating (10 K/min at RT-433 K and 2 K/min at 433-473 K)	2021 ²⁷⁾ Ikoma <i>et al</i> . 2021 ²⁸⁾
Synchrotron	Fe-Mn-Al-Si TWIP steel	Multi-pass cold-rolling (RT, equivalent strain = 2.87) + annealing (923-1373 K for 300-3600 sec)	Dislocation density	In-situ tensile $(8.3 \times 10^{-4} \text{ s}^{-1}, \text{RT})$	Bai et al. 2021 ²⁹⁾
Synchrotron	Ti/Nb composite	ARB (~8 passes with equivalent strain = 9.6, RT, 1 m/s, annealing at 848 K for 1 h between passes)	Lattice strain	In-situ tensile $(1.0 \times 10^{-3} \text{ s}^{-1}, \text{RT})$	Jiang et al. 2021 ³⁰⁾
Synchrotron	Al/Mg	HPT solid-state bonding (100 turns, <6 GPa, RT, 1 rpm)	Microstructural parameters [†] , phase fraction	Position-sensitive (0.65 mm step size for overall HPT disk surface)	Han <i>et al</i> . 2022 ³¹⁾
Synchrotron	Commercial- purity Ni	BM (150 rpm, up to 150 h) + SPS (1073 K, 30 min, 100 MPa)	Lattice strain	In-situ tensile loading (loading up to 355 MPa with 10-20 MPa loading increment)	Sjogren-Levin et al. 2023 ³²⁾
Synchrotron Neutron	Fe-Mn-C-Al TWIP steel	HPT (0, 1, 2, 3, and 5 turns, 6 GPa, RT, 1 rpm)	Texture, phase transformation (strain- dependent)	Position-sensitive (0.2 mm step size along HPT disk diameter)	Yan et al. 2014 ³³
Neutron	Al6061-T6	FSP (4.7 mm/s TR speed, 1250 rpm rotating	Texture	-	Woo et al. 2006 ³⁴⁾
Neutron	High-purity (99.99%) Al	speed, 12.4 MPa) ECAP (4 passes, route B _C at RT) & Creep (473 K under 10-50 MPa)	Texture	-	Kawasaki <i>et al.</i> 2008 ³⁵⁾
Neutron	High-purity Zr	ECAP (1 pass, 10 ⁻³ s ⁻¹ , RT)	Texture	-	Yapici <i>et al.</i> 2009 ³⁶⁾
Neutron	Al6061-T6	FSP (0.42 mm/s TR speed, 156 rpm rotating speed)	Microstructural parameters [†]	In-situ FSP	Woo et al. 2010 ³⁷⁾
Neutron	High-purity (99.99%) Cu	ECAP (1 and 8 p, route B _C)	Texture	In-situ annealing (573 K)	Ishibashi <i>et al.</i> 2013 ³⁸⁾
Neutron	Cu/Nb composite	ARB (RT until layer thicknesses down to 10-200 nm)	Texture	-	Zheng et al. 2013 ³⁹⁾ 2014 ⁴⁰⁾
Neutron	OFHC Cu	ECAP (1 pass, route B _C , RT)	Residual stress	-	Lee et al. 2017 ⁴¹
Neutron	TiAl intermetallic Compound	HPT (0, 5, and 10 turns, 6 GPa, RT, 1 rpm)	Order parameter, texture	-	Li et al. 2019 ¹²⁾
Neutron	TiAl intermetallic Compound	HPT (5 turns, 6 GPa, RT, 1 rpm)	Order parameter, phase transformation, texture	In-situ heating-cooling cycle (between 300-1350 K)	Liss <i>et al</i> . 2021 ⁴²⁾
Neutron	FeCo	HPT (1 and 4 turns, RT and 473-673 K, 6 GPa)	Order parameter	-	Glezer <i>et al</i> . 2021 ⁴³⁾
Neutron	316 SS	HPT (5 turns, 6 GPa, RT, 0.5 rpm) & annealing at 400-1173 K for 10 min	Phase change	-	Liu et al. 2022 ⁴⁴⁾
Neutron	316L SS	Additive manufacturing & HPT (15 turns, 6 GPa, RT, 1 rpm)	Microstructural parameters†, linear thermal expansion	In-situ heating (300-1240 K at 4 K/min) & cooling	Kawasaki <i>et al.</i> 2022 ⁴⁵⁾
Neutron	CoCrFeNi	Additive manufacturing & HPT (15 turns, 6 GPa, RT, 1 rpm)	Texture, microstructural parameters†, linear thermal expansion	In-situ heating (300-1240 K at 4 K/min) & cooling	Liu et al. 2023 ⁴⁶⁾

[§] SPD techniques include equal-channel angular pressing (ECAP), high-pressure torsion (HPT), accumulative roll-bonding (ARB), friction stair processing (FSP), and ball milling followed by spark plasma sintering (BM + SPS).

(i) A reduced beam size of high-energy synchrotron X-rays to micro- to nano-scales is available for probing local regions of interest with a high reciprocal space resolution providing the through-thickness microstructural information. Thus, this technique allows the mapping of heterogeneous microstructure by a series of local microstructure information for the whole bulk sample volume. An additional mechanical testing setup

[†] Microstructural parameters include coherent crystallite size, microstrain, dislocation density.

- gives further benefit to measure the local microstructural changes during the straining of the nanocrystalline samples.
- (ii) Characterization by neutron diffraction can provide time-resolved structural changes yielding structural evolution mechanisms and clarifying their transitions in bulk samples.⁴⁷⁾ It is further beneficial with the addition of other parameters including heating or cooling to characterize the real-time crystallographic changes with varying temperatures.

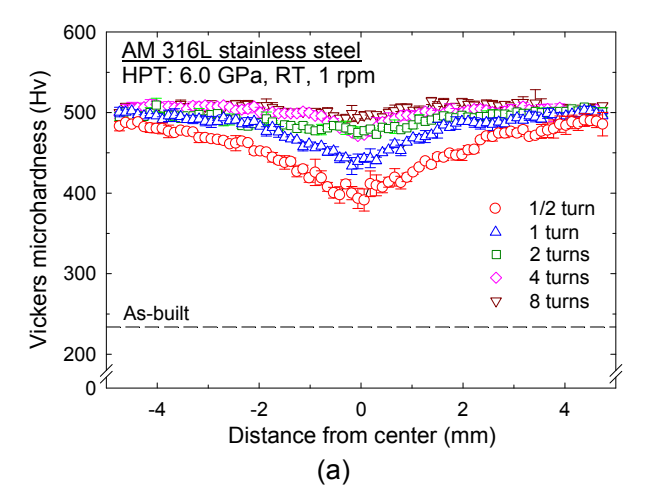
Accordingly, this overview paper provides, by describing several recent experimental results of the authors, an important insight into the microstructural transitions over temperature, time, and multiple-length scales and the characterization techniques for understanding such *in-situ* structural changes of bulk nanostructured materials processed by SPD. A special emphasis is placed on the ability and complementarity of *in-situ* observation of macro-scale microstructural evolution for hetero-nanostructured metals utilizing high-temperature laser-scanning confocal microscopy.

2. General Observations After SPD: Hardness and Structural Changes

This chapter describes the general hardness and microstructural evolution of one of the common engineering alloys, 316L stainless steel (SS), processed by HPT. Such HPTprocessed materials including the 316L SS are the base materials for describing the application of novel in-situ microstructural examinations in the following chapters. In general, these fundamental features of microstructure and mechanical properties for the HPT-processed metals are often examined and measured ex-situ through the combination of the Vickers microhardness tests, optical and electron microscopy, and lab-scale XRD. Figure 1 shows (a) the Vickers microhardness evolution across the steel disk diameter with increasing numbers of HPT rotations through 8 turns, ^{45,48)} and (b) the hardness change of the steel against shear strain, γ , introduced by HPT through 15 turns, which is given by

$$\gamma = \frac{2\pi Nr}{h} \tag{1}$$

where N is the number of HPT turn, r is the distance from the disk center of r = 0 mm, and h is the thickness of the disk sample.⁴⁹⁾ A hardness gradation within the disk diameter is visible in the alloy, especially in an early stage of HPT up to 2-4 turns, which reaches an upper limit of hardness for the steel across the disk diameter of $H_V > 500$ through 4–8 turns. The maximum hardness achieved in the alloy is about twice the initial hardness of $H_V = 233$. The hardness change regarding shear strain in Fig. 1(b) demonstrates that the hardness development of the steel during HPT follows a strain hardening model without microstructural recovery.⁵⁰⁾ As represented by the 316L stainless steel, most engineering metals and alloys demonstrate a notable hardness increase after HPT due mainly to significant grain refinement. It is well recognized by the Hall-Petch relationship⁵¹⁾ and a representative example of such hardness-grain refinement



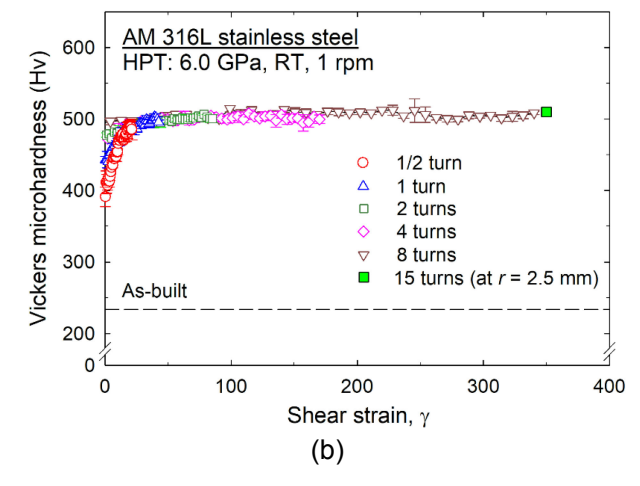


Fig. 1 (a) Vickers microhardness evolution across the steel disk diameter with increasing numbers of HPT rotations through 8 turns $^{45,48)}$ and (b) the hardness changes of the steel against shear strain, γ , introduced by HPT through 15 turns. $^{45)}$

relationship through HPT was reported for a CoCrFeNiMn high-entropy alloy (HEA) processed under 6 GPa through 2 turns.⁵²⁾ A recent report discusses the significance of different strengthening mechanisms in general engineering alloys after severe plastic deformation and the strategy to further strengthen the materials.⁵³⁾

It should be noted that the stainless steel was manufactured by an additive manufacturing (AM) approach using a laser powder bed fusion (L-PBF) technique, and the initial as-built sample had a subgrain size of 300 nm within several tens of micron-sized grains. 48) A measurement by transmission electron microscopy (TEM) revealed that the microstructure of the AM 316L steel disks achieved an average grain size of 60 nm in the equiaxed shape after 8 and higher HPT turns, 45,48) which is consistent with earlier reports on the HPT-processed 316L-grade SS regardless of manufactured conventionally by casting^{54,55)} or through AM.⁵⁶⁾ The aforementioned microstructure changes, such as nanostructuring, in bulk metals during HPT can be systematically examined ex-situ using a series of separate XRD measurements.⁹⁾ The XRD line profile taken on the surfaces of the as-built and slightly polished steel disks after HPT for different numbers of turns is shown in Fig. 2(a). 45,48) Except for a very strong 220 texture of the as-built sample,

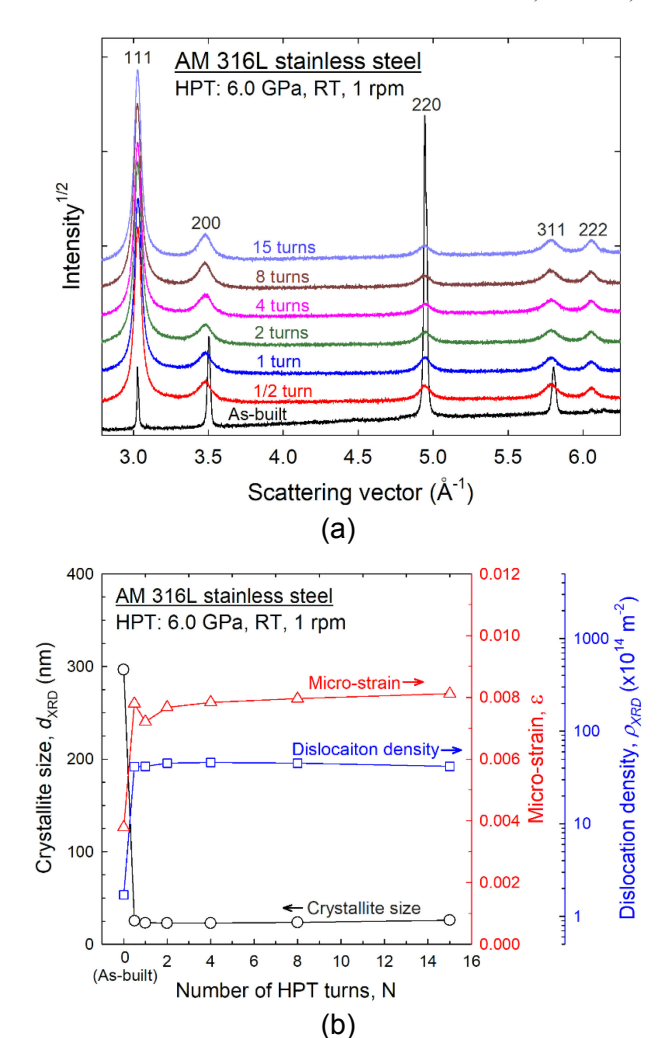


Fig. 2 (a) The XRD line profile taken on the surfaces of the as-built and slightly polished steel disks after HPT for different numbers of turns^{45,48)} and (b) the quantitative estimation of the structural parameters of crystallite size, microstrain and dislocation density with increasing HPT turns.⁴⁵⁾

which is associated with the AM procedure with the selected parameters, ⁵⁷⁾ the nanostructured steel after HPT tends to evolve the texture towards 111 through even after 1/2 turn. The developed texture is then maintained by showing visible peak broadening through 15 turns, implying severe grain refinement has occurred during HPT. The overall surface

volume demonstrated the simple f.c.c. structure without any martensitic secondary phase in the as-built sample and after HPT. A visible peak shift between the samples before and after HPT implies a lattice expansion of the f.c.c. lattices that is attributed to the introduction of excess vacancies and dislocations.⁴⁵⁾ Analysis using the Williamson-Hall method^{58,59)} enabling the quantitative estimation of the structural parameters of crystallite size d_{XRD} , microstrain ε , and dislocation density ρ_{XRD} computed by the relationship⁶⁰⁾ of $\rho = 2\sqrt{3}\langle \varepsilon^2 \rangle^{1/2}/bd$ where b is the Burgers vector and 2.58×10^{-10} m for γ -Fe⁶¹⁾ are applied in the estimation with increasing HPT turns as shown in Fig. 2(b), where N=0is equivalent to the sample in an as-built condition. ⁴⁵⁾ A consistent trend of significant change even after 1/2 HPT turn can be seen in the microstructural parameters of the AM 316 stainless steel through HPT for 15 turns.

3. In-Situ Heating Neutron Diffraction Analysis on Nanocrystalline Metals

3.1 Ultrafine-grained 316L stainless steel

Microstructural recovery of the AM 316L SS upon heating was examined in-situ upon heating from an ultrafine-grained microstructure after HPT processing by applying a neutron diffraction technique for the first time. The method of in-situ neutron scattering provided a large data set of time-resolved neutron diffractgrams during a heating-cooling cycle, which enabled the quantitative visualization of continuous microstructural parameter changes. The measurements were conducted at the iMATERIA beamline BL2062 in the Materials and Life Science Experimental Facility at the Japan Proton Accelerator Research Complex (J-PARC).⁶³⁾ The experimental setup and data correction and analysis are described in the report. The obtained neutron diffraction contour map (from Bank 1) together with a temperature change at a heating rate of 4 K/min through 1240 K are shown in Fig. 3 for the AM 316L SS after HPT for 15 turns.45)

Continuous changes in peak intensity and peak position and width at each diffraction coordinate can be visible with time, thus temperature. The high relative peak intensity is shown in red on the white profile lines in the blue background, so that the crystallographic preferred orientation, known as texture, can be estimated by the ratios of the relative peak intensities. The observed texture at t=0 min

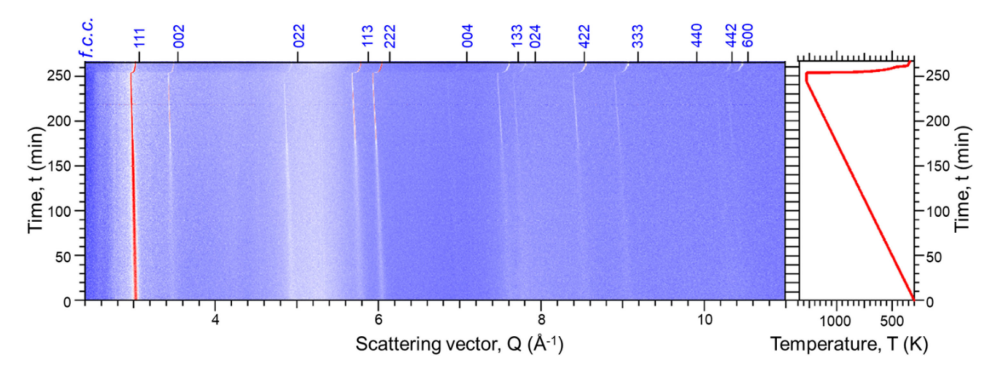


Fig. 3 Contour plots showing variation in neutron diffraction patterns of Bank 1 with time and temperature for the AM 316L SS after HPT for 15 turns. 45)

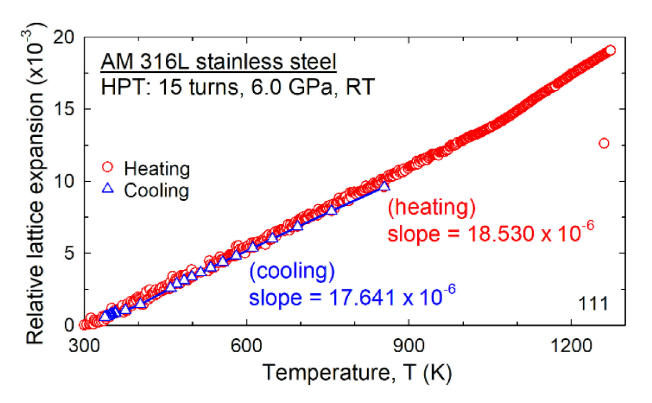


Fig. 4 Relative lattice expansion upon heating in red lines and lattice contraction upon cooling in blue lines for the HPT-processed AM 316L SS 45)

of heating is equivalent to that shown in Fig. 2(a) for the nanostructured AM steel. Through heating followed by cooling, the alloy maintained its *f.c.c.* structure without any transformation.

Apparent peak shifting upon heating and cooling indicates the lattice expansion and contraction, respectively. The relative lattice expansion and contraction through heating and cooling estimated at the strongest texture plane coordinate of 111 are shown in red and blue lines, respectively, in Fig. 4 for the HPT-processed AM 316L SS. 45 The relative values were estimated using the base value of lattice parameter, a_0 , of 3.60 Å under the minimum strain condition after completion of the heating-cooling cycle. Both thermal lattice expansion of $18.530 \times 10^{-6} \, \mathrm{K}^{-1}$ and contraction of $17.641 \times 10^{-6} \, \mathrm{K}^{-1}$ upon heating and cooling, respectively, show reasonably consistent linear relationships, and the values are consistent with the same class of steels, which typically exhibit a coefficient of thermal expansion ranging from $10 \times 10^{-6} - 20 \times 10^{-6} \, \mathrm{K}^{-1}$. 64

The relative peak width measured at the strongest texture plane coordinate of 111 with increasing temperature during the in-situ neutron measurement is shown in Fig. 5 (upper) for the HPT-processed AM 316L SS. A reduction in peak width with increasing temperature implies relaxation in microstrain and growth in crystallite size, thereby estimating the microstructural stability of the ultrafine-grained AM steel. In practice, a continuous narrowing in peak width occurred up to ~920 K, a significant drop followed between 920 and 1020 K, and it saturated at the minimum value over 1020 K. Figure 5 (upper) correlates these changes in relative peak width with the Vickers microhardness that was measured ex-situ after heating in a consistent way as the neutron measurements of the HPT-processed AM steel samples, followed by quench.⁴⁵⁾ The hardness value of $H_V > 500$ at 300 K, which is consistent with the hardness immediately after HPT of the steel shown in Fig. 1 (a) and (b), reaches the highest value of $H_V = 620$ at 873 K and decreases dramatically up to 1300 K in the nanostructured AM SS. Such hardness increase is consistent with earlier reports on conventionally manufactured 316L SS after HPT when they are heated at up to 773-873 K.54,65,66) Thus, Fig. 5 (upper) can clarify the following sequential microstructural thermal behavior at different stages of heating on the HPT-processed

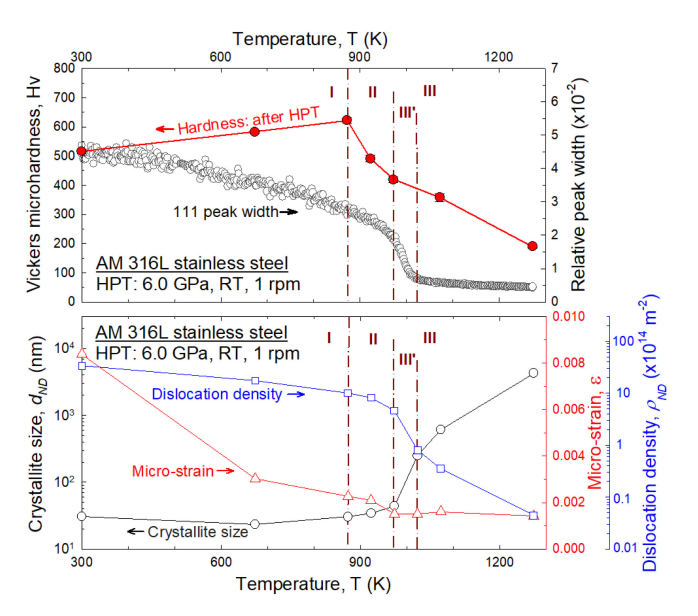


Fig. 5 (upper) Relative peak width measured at a plane coordinate of 111 and Vickers microhardness changes with increasing temperature, and (lower) structural evolution in the nanostructured AM 316L SS with heating through $1300\,\mathrm{K}^{.45)}$

AM 316L SS, which is supported by the microstructure-property relationship: (I) microstructural recovery involving micro-strain relaxation up to 873 K, (II) recrystallization with accelerated micro-strain release at 873–973 K, and (III) grain growth above 973 K including (III') completing strain relaxation in lattices up to 1023 K.

These sequential changes in the microstructural thermal behavior observed by the in-situ heating neutron diffraction measurements can be further analyzed by applying the Williamson-Hall method, for which the summary is shown in Fig. 5 (lower) including the (I)–(III) temperature regimes, showing separate microstructural thermal behavior of the HPT-processed AM 316L SS.⁴⁵⁾ The microstructural parameters of coherent crystallite size from the neutron measurement $d_{\rm ND}$, micro-strain ε , and the dislocation density $\rho_{\rm ND}$ were computed by the earlier described Williamson-Hall analysis and a relationship between these parameters. With this plot, three temperature regimes with different microstructural relaxation behavior are clearly divided by the changes in these spate microstructural parameters. Thus, stage (I) at T = 300-873 K maintains the crystallite size and dislocation density, while a significant reduction in microstrain occurs, thereby confirming microstructural recovery. It is followed by stage (II) through 973 K showing microstructural recrystallization, where the microstrain reached the minimum value without major changes in crystallite size and a small reduction in dislocation density. Above 973 K, stage (III), grain growth is apparent by the significant increase in crystallite size, whereas stage (III') at 973-1023 K in the early stage of (III) shows the completion of structural relaxation by a significant reduction in dislocation density. The novel characterization technique of in-situ heating neutron diffraction enables a comprehensive understanding of the continuous microstructural relaxation processes of bulk nanocrystalline materials. This finding supports the similar hardening behavior observed in tensile testing of a nanostructured 316 SS after 5 HPT turns under 6 GPa at 0.5 rpm, where yield stress increases up to a testing temperature of 723 K followed by softening over 723 K. 44)

The annealing-induced hardening for the SPD-processed nanomaterials is documented in a recent review article, and the following three can be the core reasons for the extra hardening during annealing and heating: (i) annihilation of mobile dislocations inside the nanograins with clustering into low energy configurations, such as low-angle grain boundaries, (ii) relaxation of non-equilibrium grain boundaries leading to a difficult emission of dislocations, and (iii) clustering of excess vacancies impeding the motion of dislocations. The current *in-situ* heating neutron diffraction experiments capture the microstructural relaxation for annealing-induced hardening favorably. The annealing-induced hardening should be differentiated from the hardening caused by phase transformations including age hardening by nucleation of precipitates.

3.2 Ultrafine-grained CoCrFeNi high-entropy alloy

Continuous microstructural recovery and relaxation behavior can be observed in any bulk nanocrystalline metals processed by severe plastic deformation under *in-situ* heating experiments. As another example of the *in-situ* heating measurement, an *f.c.c.* single-phase nearly-equiatomic 24Cr—

26Cr–25Fe–25Ni high-entropy alloy was examined by the same procedure using neutron diffraction⁴⁶⁾ after production by an AM approach⁶⁸⁾ followed by severe plastic deformation through HPT.⁶⁹⁾ The ultrafine-grained high-entropy alloy after HPT for 8 or higher numbers of turns under 6 GPa provided homogeneously distributed nanograins with average sizes of $50\sim60$ nm.

The obtained neutron diffraction contour maps from three detector banks 1-3 with temperature and time are shown in Fig. 6.46) The experiments were terminated for some time that reflected the neutron diffraction peaks of the alloy, but enough data was achieved for determining the thermal behavior of the alloy. The different detector banks orienting at peculiar scattering angles provide distinct reciprocal space probings. Except for the visible texture development during heating, the ultrafine-grained CoCrFeNi high-entropy alloy demonstrated a similar set of microstructural changes with the 316L SS, such as maintenance of f.c.c. single phase structure, an apparent reduction in the broadened peak widths during heating due to microstructural relaxation, and peak shifting describing thermal expansion and contraction with heating and cooling, respectively. After the heating-cooling cycle, a lattice parameter of $a_0 = 3.57 \,\text{Å}$ of the f.c.c. unit cell was estimated for the high-entropy alloy, that is used for the following analysis.

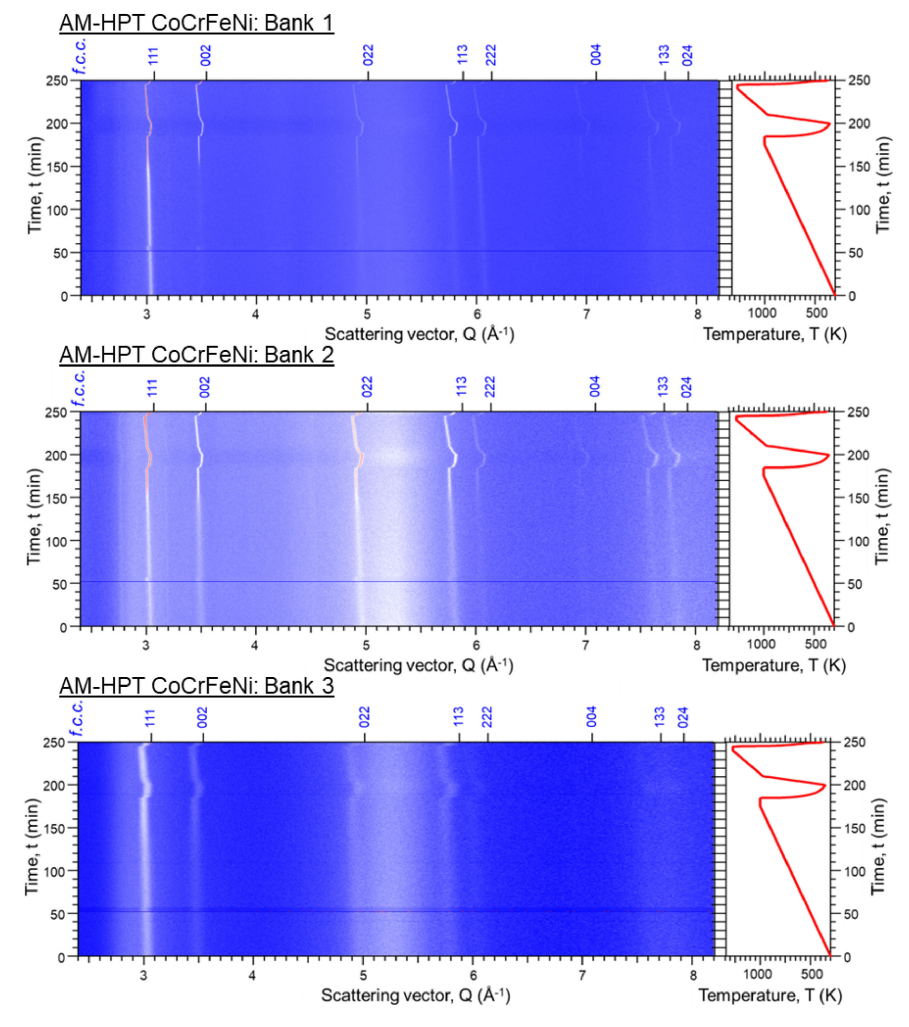


Fig. 6 Contour plots showing variation in neutron diffraction patterns from three detector banks 1–3 with time and temperature for the AM CoCrFeNi HEA after HPT for 15 turns. 46)

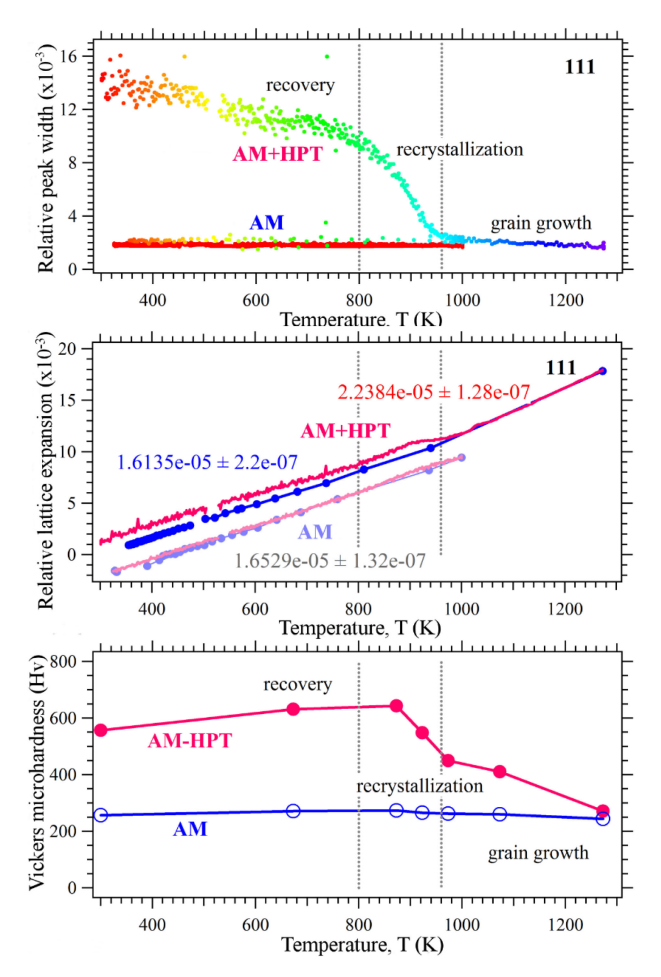


Fig. 7 Evolution of relative peak width, relative lattice expansion, and Vickers microhardness changes upon heating for both the as-printed (AM) and HPT-processed CoCrFeNi HEA.⁴⁶⁾

The neutron diffraction data for the CoCrFeNi alloy prepared by AM followed by HPT (AM-HPT) was examined in the consistent manner that was applied for the 316L steel in the previous section, and the results are summarized in Fig. 7 for the changes in, from top, relative peak width, relative lattice expansion, and Vickers microstructure with temperature. For comparison purposes, the AM sample in an as-built condition was also examined and the results are listed in the plots. While the actual numerical values are different, a consistent thermal relaxation behavior and the hardness changes during heating can be observed between the *f.c.c.* single-phase alloys of 316L SS and CoCrFeNi high-entropy alloy when comparing the plots in Figs. 4, 5(upper) and 7.

Detailed results and understanding of the thermal relaxation behavior of the ultrafine-grained high-entropy alloy in bulk volume can be found in an earlier publication. Thus, the present overview should rather emphasize the significance of the application of the novel *in-situ* heating diffraction technique for better understanding the microstructural relaxation behavior of the nanostructured material over multiple-length scales. A fine microstructure of the asbuilt CoCrFeNi high entropy alloy had a duplex microstructure consisting of elongated phases with 50–55 µm lengths which are associated with the laser spot diameter, together with equiaxed grains having <10 µm observed between neighboring tracks. ⁶⁹⁾ The alloy without nano-

crystalline microstructure failed to show any visible structural relaxation behavior, which kept the low hardness value constant through heating up to 1300 K. By contrast, as was seen in the ultrafine-grained 316L SS, continuous microstructural relaxation behaviors including the transitions of recovery, recrystallization and grain growth are captured successfully through the application of in-situ heating neutron diffraction measurements. Thus, micro-stress relaxation upon heating up to 873 K resulted in the hardness increase to the highest value of $H_V = 643$ through the microstructural recovery and recrystallization stages of the nanostructured alloy. A similar hardness increase was observed after post-HPT annealing of cast CoCrFeNiMn HEA through 723 K^{70,71)} and cast Al_{0.3}CoCrFeNi HEA through 773 K,⁷²⁾ but it is the consequence of the formation of nano-scale precipitates, which has to be differentiated from the annealing-induced hardening.⁶⁷⁾ In summary, the novel in-situ heating neutron diffraction technique is effective and practical for comprehending the microstructure-property relationships of bulk nanocrystalline materials. It lays the road-maps for making nanostructured materials not only enhancing their mechanical properties, but furthermore establishing a novel playground for drastically changed functional properties based on these heterogeneous nanostructures, such as recently observed on the inverted magnetic response in the same-reported CoCrFeNi HEA.⁷³⁾

4. Position and Strain-Dependent Phase Transformation Mapping of Diffusion-Bonded Nanocrystalline Metals by High-Energy Synchrotron X-rays

A recent success in the application of HPT technique¹⁾ includes the synthesis of bulk metastable nanocrystalline alloy through solid-state mechanical bonding of separate simple metal sheets, such as Al and Mg, by HPT at room temperature. 74-76) However, the true nano-scale grain structures with an average size of 30-40 nm together with polymorphous phase transformation under HPT and compositional heterogeneity remain challenging to observe the heterogeneous nanostructure evolution in a position-dependent manner. In practice, computer simulation and imaging techniques can visualize the microstructural evolution under HPT on dissimilar metal sheets,⁷⁷⁾ the quantitative information of compositional transition attributing to the imposed shear strain that varies with the position r within the sample given by eq. (1) is unclear with the currently available labscale measurement techniques.

Accordingly, a measurement of texture and structural mapping of a heterogeneously phase-transformed nanocrystalline Al-Mg metastable alloy was initiated using high-energy synchrotron X-ray diffraction³¹⁾ as a sophisticated tool for bulk studies. ¹⁴⁾ The material was processed by HPT for 100 turns under <6 GPa on separate Al and Mg sheets by the stacking in the order of Al/Mg/Al. The synchrotron X-ray experiment was conducted at the beamline BL02B1, SPring-8, Japan. A series of measurements taken at a separate local area of 0.2 × 0.3 mm² using micro-beam of high-energy X-rays provides numbers of separate diffraction peak profiles over the sample volume, where the schematic drawing of the sample setup and measurement locations over

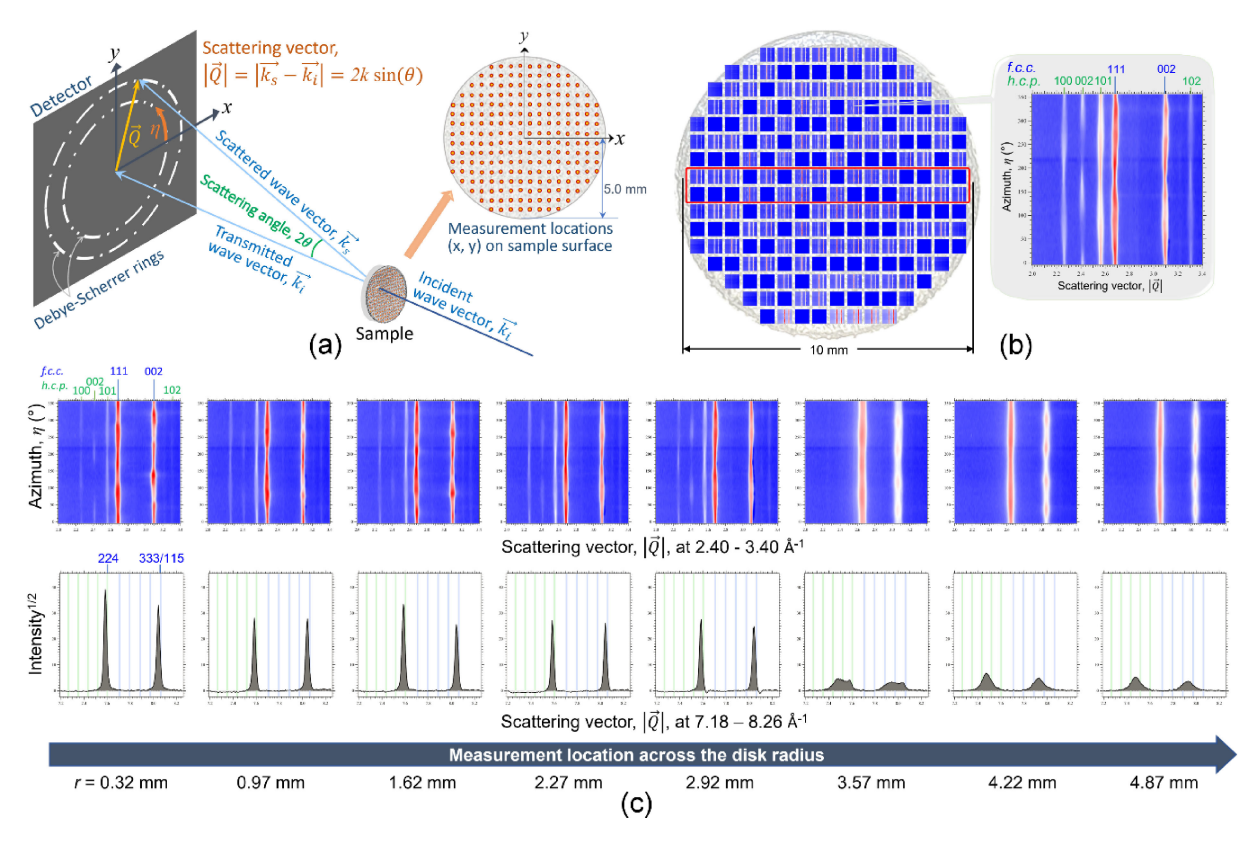


Fig. 8 (a) Schematic sample setup and the HEXD measurement locations, (b) position-dependent structure map constructed by a series of the HEXD profile with an enlarged representative diffractogram, and (c) strain/position sensitive HEXD patterns at lower $|\vec{Q}|$ (upper row) and diffractograms for a primary f.c.c. phase at higher $|\vec{Q}|$ (lower row) across the disk radius of an HPT-bonded nanocrystalline Al–Mg alloy.³¹⁾

the sample surface are shown in Fig. 8(a). High-energy X-ray diffractograms (HEXD) mapped all over the sample volume provide the feasibility of capturing gradual yet significant changes in microstructure, composition, and phases within the HPT-bonded Al–Mg nanocrystalline alloy (Fig. 8(b)). Each HEXD describes a Debye-Scherrer diffractogram along azimuth η with scattering vector \vec{Q} . An enlarged HEXD pattern taken at the mid-radius of the HPT-processed disk provides an example of a mixture of f.c.c. Al-rich and h.c.p. Mg-rich phases, and a unique set of azimuthal intensity distributions exhibit the formation of ultrafine grains having complex preferred crystallographic orientations. Pretreating the instrumental broadening, observed broadening of the diffractogram along $|\vec{Q}|$ implies broadening due to grain refinement as well as gradients in chemical composition. 74

Considering the radially symmetric microstructural development of HPT samples as implied in Fig. 1(a), a set of strain/position sensitive HEXD patterns at lower $|\vec{Q}|$ (upper row) and diffractograms for a primary f.c.c. phase at higher $|\vec{Q}|$ (lower row) are shown in Fig. 8(c) along an arbitrarily selected disk radius. Peaks at higher $|\vec{Q}|$ range can highlight peak broadening of the phase better than at lower $|\vec{Q}|$. The HEXD plots show the co-existence of f.c.c. and h.c.p. phases up to $r \approx 3$ mm. At the disk edge of r > 3 mm, phases with only f.c.c. structure are observed, and the microstructure involves nano-scale grains with high compositional gradients.

By connecting the measurement position and the HPT-induced shear strain γ expressed by eq. (1), this measurement can evaluate the processing-microstructure relationship of

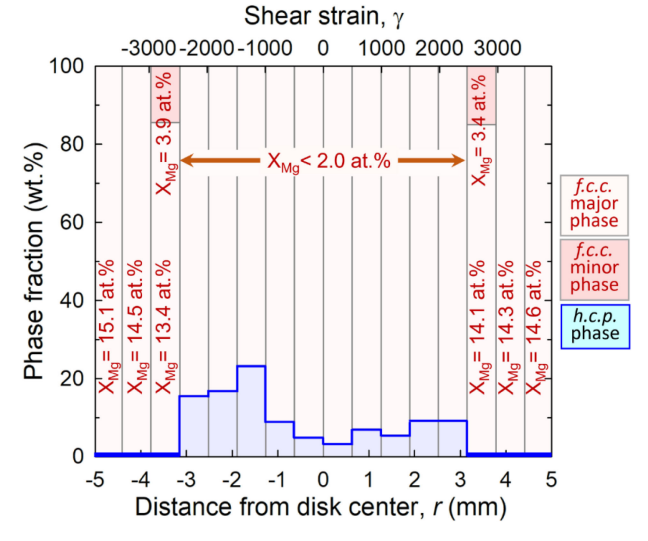


Fig. 9 Phase fractions of the *f.c.c.* and *h.c.p.* phases observed by the HEXD experiments evaluated along the disk diameter of the HPT-bonded Al–Mg alloy.³¹⁾

the severely deformed nanocrystalline Al–Mg alloy involving significant phase transformation. Specifically, compositional broadening of the HEXD diffractogram was quantitatively analyzed across the HPT disk diameter, and the results are plotted in phase fraction of the *f.c.c.* and *h.c.p.* phases vs. distance from disk center, which stands for the imposed shear strain during HPT (Fig. 9).³¹⁾ The results summarize the dependence of the HPT-induced Al/Mg mechanical bonding

on position-sensitive accumulated shear strain leading to different degrees of phase transformation from separate f.c.c. and h.c.p. phases up to $\gamma=2500$ to ultimately a supersaturate solid solution f.c.c. phase with 14–15 at% Mg in Al at $3000 < \gamma < 4000$. This study demonstrates the excellent potential of the characterization technique using high-energy synchrotron X-ray diffraction for visualizing gradual microstructural changes and phase transformation in heterogeneously nanostructured metallic materials. It is worth noting that the first position-sensitive high-energy synchrotron X-ray measurement on an HPT-processed sample was conducted along the disk diameter after 1 turn of an Fe–Mn–C–Al TWIP steel that was further examined by neutron diffraction to evaluate phase transformation with increasing HPT turns to 5 turns at 6 GPa. 33

5. *In-Situ* Laser-Scanning Confocal Microscopy for Observing Macro-Scale Microstructural Changes Upon Heating

Besides the novel diffraction techniques explained in earlier sections, optical microscopy and electron microscopy have been serving as indispensable and complementary techniques for metallurgy and materials science research. Various microscopy techniques have been accepted to date for advancing nanocrystalline materials research, ²⁻⁵⁾ and the ability to analyze at higher resolution is essential to examine a variety of planar defects in nanocrystalline materials. Accordingly, appropriate microscopy techniques have to be selected by considering not only the objects of investigation (grain size, morphology and grain boundary, twin boundaries, dislocations, texture, etc.) but also the time-dependent evolution of the objects under specific conditions (temperature, pressure, stress, corrosion, etc.). Thus, considering the correlation between in-situ heating (Section 3) and heterogeneous structural evolution and phase transformation (Section 4) observed in the bulk nanocrystalline metals processed by HPT, this section describes a novel microscopy technique of laser-scanning confocal microscopy (LSCM) used with a heating facility that allows in-situ observations of micron-scale heterogeneous microstructural evolution.

LSCM uses laser as a light source and applies pin-hole technology enabling high-resolution observation at high temperatures not being affected by thermal radiation. However, when it comes to the visual observation made at the surface, unlike other techniques that use a signal from bulk, an effort should be made to ensure the surface observation of an event is representative of bulk behavior. For instance, avoiding oxidation on the surface of the HEA specimen is essential, which requires an extra level of the protective environment in order not to obtain misleading information. Nevertheless, some oxidation may still occur at higher temperatures, but in the present case, it was sensitive to the underlying phase structure, still suitable to determine the different regimes of microstructure and phase evolution

The thermal behavior of a nanocrystalline CoCrFeNiMn HEA after HPT was examined *in-situ* by LSCM with a heating system. High-temperature LSCM has been widely used to make observations of solidification morphology,

phase transformation, microstructural relaxation, precipitation, etc., and to examine the mechanism and kinetics of such. A schematic drawing and principles of confocal optics and infrared heating system as well as examples of earlier studies on metallic materials are found elsewhere. An HPT-processed nanocrystalline CoCrFeNiMn HEA disk having 10 mm diameter and ~0.7 mm thickness was cut vertically and mirror polished, to examine the microstructure close to the disk edge on the vertical cross-section. Using a high-temperature LSCM (Model VL2000DX-SVF18SP) observations were made during heating from 373 K to 923 K at a rate of 10 K/min followed by rapid cooling with a quenching gas.

The CoCrFeNiMn HEA is one of the well-studied *f.c.c.* single-phase HEA, and it has reasonably similar nanocrystal-line microstructure and hardness to a four-element CoCrFeNi HEA after HPT processing. Saturated nano-scale grains with an average size of 40–50 nm are observed in the CoCrFeNiMn HEA earlier, 52,70,82) and a phase transformation is expected when isothermally held at 723 K for 1–10 hours, 70,71,83) while such phase transformation has not been observed in the four-element CoCrFeNi alloy through 1000 K⁸⁴) and 1300 K as shown in Fig. 6.⁴⁶)

Figure 10 shows a series of LSCM micrographs taken at a consistent disk edge region of the HPT-processed CoCrFeNiMn HEA at arbitrarily selected temperatures. At 373-580 K the overall microstructure was homogenous without any trace of large-scale microstructural change at the measurement scale, while above 580 K a multi-phase and elongated microstructure that follows a shear direction was developed in the regions of 150-200 um from the top and bottom disk surfaces except for the disk middle-section. The developed multi-phase regions near the top and bottom of the disk surfaces were clearly recognized in the observation thanks to the contrast difference between neighboring phases. This structure - the combination of multi-phase close to the disk surfaces and single-phase type microstructure at the middle of the disk section - was maintained reasonably up to 680 K. Over 680 K up to 900 K, the disk middle-section appears to adopt the multi-phase microstructure, but the morphology of the multi-phases appears rather equiaxed at the middle-section than elongated along the shear pattern that is found at the disk surface regions. This difference can be clearly confirmed in the higher magnification micrograph taken around the border (denoted with a yellow dot line) of these two regions at 793.2 K, where the upper half shows more equiaxed phases while the lower half displays the elongated phases. At temperatures over 900 K the overall multi-phase microstructure appeared homogeneous with reasonably coarse and equiaxed phase morphology and the structure was maintained toward room temperature after rapid cooling.

This preliminary experiment obtained by the high-temperature LSCM shows the heterogeneous microstructural evolution within the nanostructured HEA disk upon heating for the first time. It is well consistent and anticipated by the nature of HPT creating heterogeneous straining not only along the disk perimeter but also along the disk height⁸⁵⁾ leading to microstructural heterogeneity between the regions close to the disk surfaces and the middle-section.¹²⁾ The

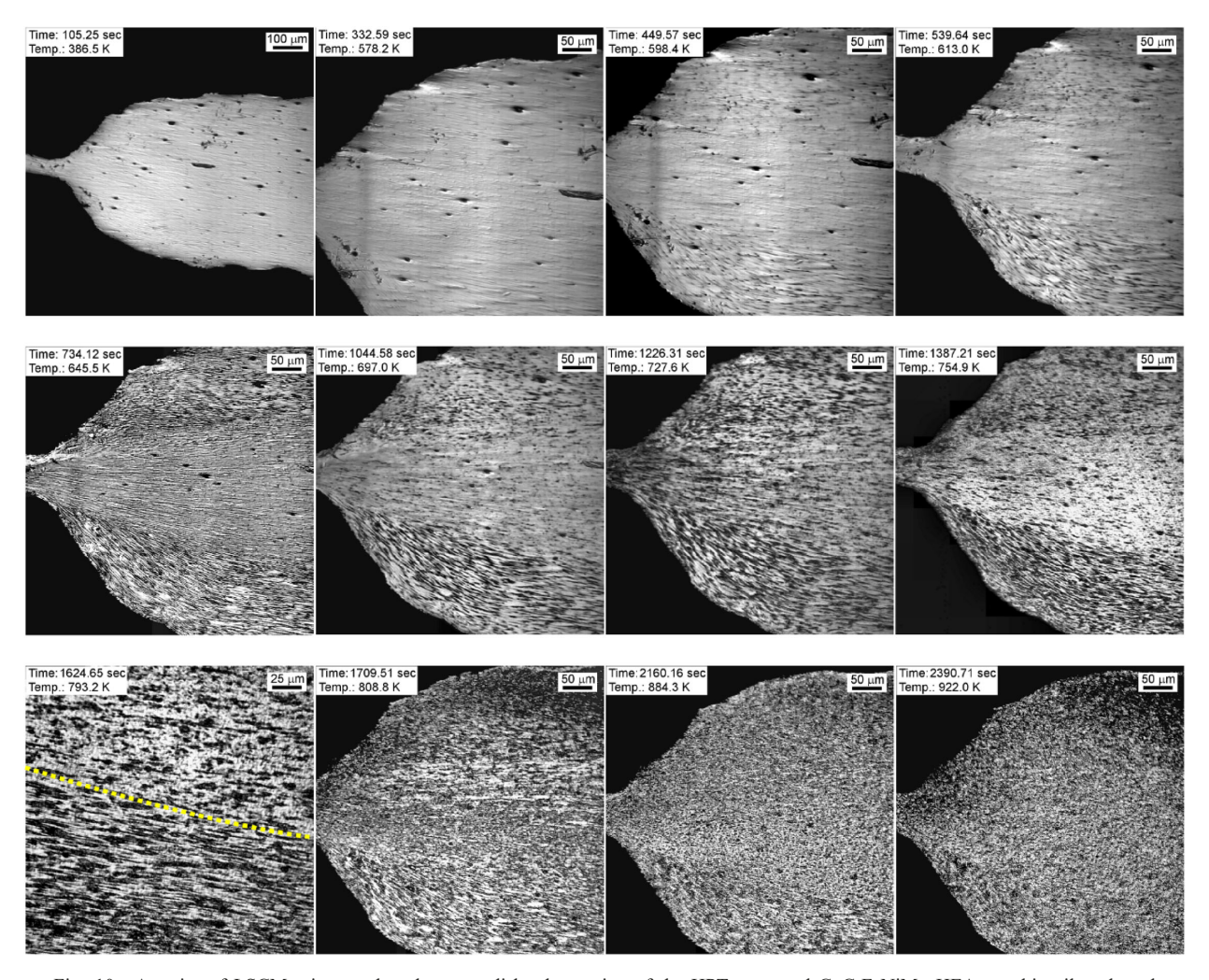


Fig. 10 A series of LSCM micrographs taken at a disk edge region of the HPT-processed CoCrFeNiMn HEA at arbitrarily selected temperatures between 373 K and 923 K. A yellow dot line in a micrograph taken at 793.2 K denotes a border separating the regions with different phase morphology.

hierarchical formation of multi-phase microstructure in the nanostructured HEA upon heating implies that the peak hardness for the CoCrFeNiMn HEA^{70,71,83)} for which the reported phase transformation temperature of 723 K is responsible, might have been measured within the middle-section of the disk samples.

Although the applied magnification in the present study is impracticable in resolving the nano-scale grain and phase sizes, visualization of heterogeneous microstructural evolution upon heating over such a large area of the sample brings a significant contribution to understanding the thermal stability of the bulk nanostructured and hetero-structured metals. In addition to this benefit, by complementing this technique with other techniques, the journey of investigation can be made efficient. While the high-temperature LSCM has been utilized to support the results achieved by *in-situ* heating neutron diffraction analysis often for identifying the phase transformation of metallic materials, 15,86,87) it can be used in a way and vice versa as a preliminary step prior to employing time-intensive techniques such as TEM, atom probe tomography, nanoindentation, etc. which essentially involve dedicated sample preparations and efforts for identifying the regions of interest.

6. Summary and Conclusion

This overview paper is aimed to provide several recent examples of utilizing novel diffraction and microscopy techniques that can be utilized complementarily for the characterization of bulk nanostructured metals processed by severe plastic deformation, specifically HPT. In practice, the following findings and conclusions are derived from the described techniques and analysis methods.

- (1) In-situ heating neutron diffraction examinations were conducted to examine the microstructural relaxation of the nanostructured 316L SS and CoCrFeNi HEA after HPT. Sequential microstructural relaxation features can be paired with the mechanical testing results for a better understanding of the minutely changing microstructure-property relationship of the nanocrystalline metals.
- (2) Micro-beam of synchrotron high-energy X-rays enabled the localized microstructural measurements over the sample volume of an HPT-bonded Al-Mg nanocrystalline alloy. Mapping of the local HEXD peaks over the sample exhibits detailed compositional changes with different imposed strains leading to the comprehension

- of the processing-microstructure relationship for nanocrystalline and hetero-structured metals.
- (3) High-temperature laser-scanning confocal microscopy (LSCM) provided *in-situ* heating microscopic observation on a CoCrFeNiMn HEA after HPT. The observations made with the variation of temperature enabled the visualization of hierarchical phase transformation which is dependent on the location within the bulk nanostructured sample. This characterization method may be an excellent preliminary characterization technique for more involved *in-* and *ex-situ* nano-scale microstructural and mechanical testing.

Acknowledgments

This study was supported in part by the National Science Foundation of the United States under Grant No. CMMI-2051205 (M.K.). The authors greatly acknowledge the Ibaraki prefectural government and the J-PARC facility for granting access to iMATERIA under the 2019 Overseas Academic User Program of Ibaraki Neutron Beamline BL20, proposal number 2019PM2014. The authors acknowledge the Japan Synchrotron Radiation Research Institute for granting beam time and logistics on beamline BL02B1 at SPring 8 under Proposal No. 2018B1219. The authors acknowledge the University of Wollongong for granting access to facilities in the High-temperature Microscopy Laboratory.

REFERENCES

- 1) K. Edalati et al.: Mater. Res. Lett. 10 (2022) 163-256.
- 2) G. McMahon and T. Malis: Microsc. Res. Tech. 31 (1995) 267-274.
- X. Sauvage, W. Lefebvre, C. Genevois, S. Ohsaki and K. Hono: Scr. Mater. 60 (2009) 1056–1061.
- M. Seyring, X. Song and M. Rettenmayr: ACS Nano 5 (2011) 2580– 2586
- A. Kobler, A. Kashiwar, H. Hahn and C. Kubel: Ultramicroscopy 128 (2013) 68–81.
- 6) E. Schafler and M. Zehetbauer: Rev. Adv. Mater. Sci. 10 (2005) 28-33.
- 7) T. Ungár: J. Mater. Sci. 42 (2007) 1584-1593.
- 8) J. Gubicza and T. Ungár: Z. Kristallogr. 222 (2007) 567-579.
- M.B. Kerber, M.J. Zehetbauer, E. Schaffer, F.C. Spieckermann, S. Bernstorff and T. Ungar: JOM 63 (2011) 61–70.
- N.S. De Vincentis, M.C. Avalos, E.A. Benatti, A. Kliauga, H.G. Brokmeier and R.E. Bolmaro: Mater. Charact. 123 (2017) 137–152.
- H.-J. Lee, S.K. Lee, K.H. Jung, G.A. Lee, B. Ahn, M. Kawasaki and T.G. Langdon: Mater. Sci. Eng. A 630 (2015) 90–98.
- X. Li, R.J. Dippenaar, J.-K. Han, M. Kawasaki and K.-D. Liss: J. Alloy. Compd. 787 (2019) 1149–1157.
- 13) K.-D. Liss: Quantum Beam Sci. 1 (2017) 1.
- 14) K.-D. Liss, A. Bartels, A. Schreyer and H. Clemens, Textures Microstruct. 35 (2003) 219–252.
- I.J. Watson, K.-D. Liss, H. Clemens, W. Wallgram, T. Schmoelzer, T.C. Hansen and M. Reid: Adv. Eng. Mater. 11 (2009) 932–937.
- 16) K.D. Liss, R.E. Whitfield, W. Xu, T. Buslaps, L.A. Yeoh, X. Wu, D. Zhang and K. Xia: J. Synchrotron Radiat. 16 (2009) 825–834.
- H. Azzeddine, B. Mehdi, L. Hennet, D. Thiaudière, B. Alili, M. Kawasaki, D. Bradai and T.G. Langdon: Mater. Sci. Eng. A 597 (2014) 288–294.
- 18) A. Panigrahi, M. Bönisch, T. Waitz, E. Schafler, M. Calin, J. Eckert, W. Skrotzki and M. Zehetbauer: J. Alloy. Compd. 628 (2015) 434–441.
- C. Reyes-Ruiz, I.A. Figueroa, C. Braham, J.M. Cabrera, O. Zanellato,
 S. Baiz and G. Gonzalez: Mater. Sci. Eng. A 670 (2016) 227–232.
- 20) H. Adachi, Y. Karamatsu, S. Nakayama, T. Miyazawa, M. Sato and T.

- Yamasaki: Mater. Trans. 57 (2016) 1447-1453.
- E. Schafler, M.B. Kerber, F. Spieckermann, T. Fischer, R. Schuster and C. von Baeckmann: Magnesium Technology 2017, (2017) pp. 645– 651.
- 22) K.S. Kormout, P. Ghosh, A. Bachmaier, A. Hohenwarter and R. Pippan: Acta Mater. 154 (2018) 33-44.
- B. Schuh, B. Völker, J. Todt, N. Schell, L. Perrière, J. Li, J.P. Couzinié and A. Hohenwarter: Acta Mater. 142 (2018) 201–212.
- 24) B.B. Straumal, A.R. Kilmametov, B. Baretzky, O.A. Kogtenkova, P.B. Straumal, L. Lityńska-Dobrzyńska, R. Chulist, A. Korneva and P. Zieba: Acta Mater. 195 (2020) 184–198.
- S. Wurster, M. Stückler, L. Weissitsch, T. Müller and A. Bachmaier: Appl. Sci. 10 (2020) 5094.
- R. Sonkusare, K. Biswas, N. Al-Hamdany, H.G. Brokmeier, R. Kalsar,
 N. Schell and N.P. Gurao: Mater. Sci. Eng. A 782 (2020) 139187.
- K. Bartha, J. Stráský, P. Barriobero-Vila, J. Šmilauerová, P. Doležal, J. Veselý, I. Semenova, V. Polyakova and M. Janeček: J. Alloy. Compd. 867 (2021) 159027.
- Y. Ikoma, T. Yamasaki, T. Masuda, Y. Tange, Y. Higo, Y. Ohishi, M.R. McCartney, D.J. Smith and Z. Horita: Philos. Mag. Lett. 101 (2021) 223–231.
- Y. Bai, H. Kitamura, S. Gao, Y. Tian, N. Park, M.H. Park, H. Adachi, A. Shibata, M. Sato, M. Murayama and N. Tsuji: Sci. Rep. 11 (2021) 15870.
- S. Jiang, R.L. Peng, Z. Hegedűs, T. Gnäupel-Herold, J.J. Moverare, U. Lienert, F. Fang, X. Zhao, L. Zuo and N. Jia: Acta Mater. 205 (2021) 116546
- J.-K. Han, K. Sugimoto, M. Kawasaki and K.-D. Liss: Mater. Lett. 321 (2022) 132414.
- E. Sjögren-Levin, W. Pantleon, A. Ahadi, Z. Hegedüs, U. Lienert, N. Tsuji, K. Ameyama and D. Orlov: Scr. Mater. 226 (2023) 115186.
- 33) K. Yan, D. Bhattacharyya, Q. Lian, S. Kabra, M. Kawasaki, D.G. Carr, M.D. Callaghan, M. Avdeev, H. Li, Y. Wang, X. Liao, T.G. Langdon, K.-D. Liss and R.J. Dippenaar: Adv. Eng. Mater. 16 (2014) 927–932.
- 34) W. Woo, H. Choo, D. Brown, S. Vogel, P. Liaw and Z. Feng: Acta Mater. 54 (2006) 3871–3882.
- M. Kawasaki, I.J. Beyerlein, S.C. Vogel and T.G. Langdon: Acta Mater.
 (2008) 2307–2317.
- G.G. Yapici, C.N. Tomé, I.J. Beyerlein, I. Karaman, S.C. Vogel and C. Liu: Acta Mater. 57 (2009) 4855–4865.
- W. Woo, T. Ungár, Z. Feng, E. Kenik and B. Clausen: Metall. Mater. Trans. A 41 (2010) 1210–1216.
- T. Ishibashi, Y. Tomota, S. Sugaya, H. Toyokawa, T. Hirade, Z. Horita and H. Suzuki: Mater. Trans. 54 (2013) 1562–1569.
- S. Zheng, I.J. Beyerlein, J.S. Carpenter, K. Kang, J. Wang, W. Han and N.A. Mara: Nat. Commun. 4 (2013) 1696.
- S. Zheng, J.S. Carpenter, R.J. McCabe, I.J. Beyerlein and N.A. Mara: Sci. Rep. 4 (2014) 4226.
- 41) H.H. Lee, K.D. Gangwar, K.-T. Park, W. Woo and H.S. Kim: Mater. Sci. Eng. A 682 (2017) 691–697.
- K.-D. Liss, X. Liu, X. Li, J.-K. Han, R.J. Dippenaar and M. Kawasaki: Mater. Lett. 304 (2021) 130650.
- 43) A.M. Glezer, L.F. Muradimova, P.A. Borisova, A.A. Veligzhanin, O.V. Chernysheva, R.V. Sundeev, D.V. Louzguine-Luzgin, N.S. Perov, S.O. Shirshikov and A.A. Tomchuk: J. Alloy. Compd. 866 (2021) 159021.
- 44) M. Liu, W. Gong, R. Zheng, J. Li, Z. Zhang, S. Gao, C. Ma and N. Tsuji: Acta Mater. 226 (2022) 117629.
- 45) M. Kawasaki, J.-K. Han, X. Liu, Y. Onuki, Y.O. Kuzminova, S.A. Evlashin, A.M. Pesin, A.P. Zhilyaev and K.-D. Liss: Adv. Eng. Mater. 24 (2022) 2100968.
- 46) X. Liu, J.-K. Han, Y. Onuki, Y.O. Kuzminova, S.A. Evlashin, M. Kawasaki and K.-D. Liss: Adv. Eng. Mater. 25 (2023) 2201256.
- 47) K.-D. Liss: Metals 7 (2017) 266.
- J.-K. Han, X. Liu, I. Lee, Y.O. Kuzminova, S.A. Evlashin, K.-D. Liss and M. Kawasaki: Mater. Lett. 302 (2021) 130364.
- 49) A.P. Zhilyaev and T.G. Langdon: Prog. Mater. Sci. 53 (2008) 893–979.
- 50) M. Kawasaki: J. Mater. Sci. 49 (2014) 18-34.
- 51) E.O. Hall: Proc. Phys. Soc. London Sect. B **64** (1951) 742–747.
- D.-H. Lee, I.-C. Choi, M.-Y. Seok, J. He, Z. Lu, J.-Y. Suh, M. Kawasaki, T.G. Langdon and J.-i. Jang: J. Mater. Res. 30 (2015) 2804–2815.

- S. Dangwal, K. Edalati, R.Z. Valiev and T.G. Langdon: Crystals 13 (2023) 413.
- 54) S. Scheriau, Z. Zhang, S. Kleber and R. Pippan: Mater. Sci. Eng. A 528 (2011) 2776–2786.
- J. Gubicza, M. El-Tahawy, Y. Huang, H. Choi, H. Choe, J.L. Lábár and T.G. Langdon: Mater. Sci. Eng. A 657 (2016) 215–223.
- S. Mohd Yusuf, Y. Chen, S. Yang and N. Gao: Mater. Charact. 159 (2020) 110012.
- H. Choo, K.-L. Sham, J. Bohling, A. Ngo, X. Xiao, Y. Ren, P.J. Depond, M.J. Matthews and E. Garlea: Mater. Des. 164 (2019) 107534.
- 58) G.K. Williamson and W.H. Hall: Acta Metall. Mater. 1 (1953) 22-31.
- 59) E.J. Mittemeijer and U. Welzel: Z. Kristallogr. 223 (2008) 552-560.
- 60) G.K. Williamson and R.E. Smallman: Philos. Mag. 1 (1956) 34-46.
- H.J. Frost and M.F. Ashby: Deformation-Mechanism Maps: The Plasticity and Creep of Metals and Ceramics, (Pergamon Press, New York, Oxford, 1982).
- T. Ishigaki et al.: Nucl. Instrum. Methods Phys. Res. A 600 (2009) 189–191.
- 63) K. Nakajima et al.: Quantum Beam Sci. 1 (2017) 9.
- B. Brink, K. Stahl, T.L. Christiansen and M.A.J. Somers: J. Appl. Crystallogr. 47 (2014) 819–826.
- H. Wang, I. Shuro, M. Umemoto, K. Ho-Hung and Y. Todaka: Mater. Sci. Eng. A 556 (2012) 906–910.
- 66) M. El-Tahawy, Y. Huang, T. Um, H. Choe, J.L. Lábár, T.G. Langdon and J. Gubicza: J. Mater. Res. Technol. 6 (2017) 339–347.
- 67) J. Gubicza: Adv. Eng. Mater. 22 (2020) 1900507.
- 68) Y. Kuzminova, D. Firsov, A. Dudin, S. Sergeev, A. Zhilyaev, A. Dyakov, A. Chupeeva, A. Alekseev, D. Martynov, I. Akhatov and S. Evlashin: Intermetallics 116 (2020) 106651.
- 69) W. Zhao, J.-K. Han, Y.O. Kuzminova, S.A. Evlashin, A.P. Zhilyaev, A.M. Pesin, J.-i. Jang, K.-D. Liss and M. Kawasaki: Mater. Sci. Eng. A 807 (2021) 140898.
- B. Schuh, F. Mendez-Martin, B. Völker, E.P. George, H. Clemens, R. Pippan and A. Hohenwarter: Acta Mater. 96 (2015) 258–268.

- V. Maier-Kiener, B. Schuh, E.P. George, H. Clemens and A. Hohenwarter: Mater. Des. 115 (2017) 479–485.
- Q.H. Tang, Y. Huang, Y.Y. Huang, X.Z. Liao, T.G. Langdon and P.Q. Dai: Mater. Lett. 151 (2015) 126–129.
- A. Paul, X. Liu, M. Kawasaki and K.-D. Liss: Appl. Phys. Lett. 122 (2023) 052402.
- 74) J.K. Han, K.D. Liss, T.G. Langdon and M. Kawasaki: Sci. Rep. 9 (2019) 17186.
- J.-K. Han, K.-D. Liss, T.G. Langdon, J.-i. Jang and M. Kawasaki: Mater. Sci. Eng. A 796 (2020) 140050.
- J.-K. Han, T. Herndon, J.-i. Jang, T.G. Langdon and M. Kawasaki: Adv. Eng. Mater. 22 (2020) 1901289.
- M. Pouryazdan, B.J.P. Kaus, A. Rack, A. Ershov and H. Hahn: Nat. Commun. 8 (2017) 1611.
- 78) S.-C. Moon, D. Phelan and R. Dippenaar: Mater. Charact. 172 (2021) 110841.
- H. Shibata, Y. Arai, M. Suzuki and T. Emi: Metall. Mater. Trans. B 31 (2000) 981–991.
- 80) M. Reid, D. Phelan and R. Dippenaar: ISIJ Int. 44 (2004) 565-572.
- J. Gubicza, P.T. Hung, M. Kawasaki, J.-K. Han, Y. Zhao, Y. Xue and J.L. Lábár: Mater. Charact. 154 (2019) 304–314.
- D.-H. Lee, I.-C. Choi, G. Yang, Z. Lu, M. Kawasaki, U. Ramamurty, R. Schwaiger and J.-i. Jang: Scr. Mater. 156 (2018) 129–133.
- 83) D.-H. Lee, J.-A. Lee, Y. Zhao, Z. Lu, J.-Y. Suh, J.-Y. Kim, U. Ramamurty, M. Kawasaki, T.G. Langdon and J.-i. Jang: Acta Mater. 140 (2017) 443–451.
- 84) P.T. Hung, M. Kawasaki, J.-K. Han, J.L. Lábár and J. Gubicza: Mater. Charact. 171 (2021) 110807.
- 85) R. Kulagin, Y. Beygelzimer, Y. Ivanisenko, A. Mazilkin and H. Hahn: IOP Conf Ser: Mater Sci. Eng. 194 (2017) 012045.
- K.D. Liss, A. Stark, A. Bartels, H. Clemens, T. Buslaps, D. Phelan and L.A. Yeoh: Adv. Eng. Mater. 10 (2008) 389–392.
- S. Kabra, K. Yan, D.G. Carr, R.P. Harrison, R.J. Dippenaar, M. Reid and K.-D. Liss: J. Appl. Phys. 113 (2013) 063513.